

1 **High-resolution surface velocities and strain for Anatolia from Sentinel-1**

2 **InSAR and GNSS data**

3

4 Jonathan R. Weiss^{1,2*}, Richard J. Walters³, Yu Morishita^{1,4}, Tim J. Wright¹, Milan Lazecky¹, Hua
5 Wang⁵, Ekbal Hussain⁶, Andrew J. Hooper¹, John R. Elliott¹, Chris Rollins¹, Chen Yu¹⁰, Pablo J.
6 González^{7,8}, Karsten Spaans⁹, Zhenhong Li¹⁰, and Barry Parsons¹¹

7

8 ¹COMET, School of Earth and Environment, University of Leeds, United Kingdom

9 ²Institute of Geosciences, University of Potsdam, Germany

10 ³COMET, Department of Earth Sciences, University of Durham, United Kingdom

11 ⁴Geospatial Information Authority of Japan, Tsukuba, Japan

12 ⁵Department of Surveying Engineering, Guangdong University of Technology, Guangzhou,
13 China

14 ⁶British Geological Survey, Natural Environment Research Council, United Kingdom

15 ⁷COMET, Department of Earth, Ocean and Ecological Sciences, University of Liverpool, United
16 Kingdom

17 ⁸Volcanology Research Group, Department of Life and Earth Sciences, IPNA-CSIC, Spain

18 ⁹SatSense, Leeds, United Kingdom

19 ¹⁰COMET, School of Engineering, Newcastle University, United Kingdom

20 ¹¹COMET, Department of Earth Sciences, University of Oxford, United Kingdom

21

22 *Correspondence to: jonathan.weiss@uni-potsdam.de

23

24 **Key Points:**

- 25 • We produce high-resolution horizontal and vertical velocity and strain rate fields for Anatolia
26 from Sentinel-1 and GNSS observations
- 27 • Velocity gradients indicate shear strain accumulation along the North and East Anatolian
28 Faults and extension across western Anatolia
- 29 • InSAR data are critical for capturing high-resolution details of the velocity and strain rate
30 field

31

32 **Abstract**

33 Measurements of present-day surface deformation are essential for the assessment of long-
34 term seismic hazard. The European Space Agency's Sentinel-1 satellites enable global, high-
35 resolution observation of crustal motion from Interferometric Synthetic Aperture Radar (InSAR).
36 We have developed new automated InSAR processing systems that exploit the first ~5 years of
37 Sentinel-1 data to measure surface motions for the ~800,000 km² Anatolian region. Our new 3D
38 velocity and strain rate fields illuminate deformation patterns dominated by westward motion of
39 Anatolia relative to Eurasia, localized strain accumulation along the North and East Anatolian
40 Faults, and rapid vertical signals associated with anthropogenic activities and to a lesser extent
41 extension across the grabens of western Anatolia. We show that automatically processed
42 Sentinel-1 InSAR can characterize details of the velocity and strain rate fields with high
43 resolution and accuracy over large regions. These results are important for assessing the
44 relationship between strain accumulation and release in earthquakes.

45

46 **Plain Language Summary**

47 Satellite-based measurements of small rates of motion of the Earth's surface made at high
48 spatial resolutions and over large areas are important for many geophysical applications
49 including improving earthquake hazard models. We take advantage of recent advances in
50 geodetic techniques in order to measure surface velocities and tectonic strain accumulation
51 across the Anatolia region, including the highly seismogenic and often deadly, North Anatolian
52 Fault. We show that by combining Sentinel-1 Interferometric Synthetic Aperture Radar (InSAR)
53 data with Global Navigation Satellite System (GNSS) measurements we can enhance our view of
54 surface deformation associated with active tectonics, the earthquake cycle, and anthropogenic
55 processes.

56

57 **1. Introduction**

58 Geodetic measurements of crustal motion are crucial for understanding the earthquake cycle
59 [e.g. *Elliott et al.*, 2016; *Hearn*, 2003; *Smith and Sandwell*, 2006; *Wright*, 2016; *Wright et al.*,
60 2001], characterizing spatial variations in lithospheric rheology and fault frictional properties
61 [e.g. *Jolivet et al.*, 2013; *Lindsey et al.*, 2014; *Weiss et al.*, 2019], and illuminating the mechanics
62 of large-scale continental deformation [e.g. *England et al.*, 2016; *Loveless and Meade*, 2011;
63 *Walters et al.*, 2017]. Satellite-based geodetic data are also becoming an increasingly important
64 component of efforts to assess earthquake hazard [e.g. *Chaussard et al.*, 2015; *Kreemer et al.*,
65 2014] as many major faults exhibit focused and measurable strain at the surface during the
66 interseismic period [*Wei et al.*, 2010; *Wright et al.*, 2004b; *Wright et al.*, 2013].

67

68 Geodetic strain rate measurements can be related to seismicity rates [e.g. *Bird et al.*, 2015;
69 *Molnar*, 1979; *Rollins and Avouac*, 2019]. However, global and regional strain rate models

70 usually rely on Global Navigation Satellite System (GNSS) velocity measurements, and these
71 often have insufficient density in many countries at risk from earthquakes, particularly in the
72 Alpine-Himalayan Belt. Even in well-instrumented regions such as California and Japan, the
73 typical spacing between GNSS observation points of 10-50 km may still be insufficient to
74 resolve strain localization at the scale necessary to distinguish between faults that are locked at
75 the surface and those that are creeping aseismically [Elliott *et al.*, 2016]. The gaps in GNSS
76 coverage are likely to persist and they have a major effect on the corresponding estimates of
77 strain rate; regions of inferred high strain rate are controlled by the distribution of observations,
78 potentially resulting in inaccuracies. Furthermore, temporal variations in strain accumulation
79 around active faults may go undetected if velocities and strain-rates are based on old or non-
80 continuous observations [Bilham *et al.*, 2016; Cetin *et al.*, 2014; Rousset *et al.*, 2016].

81
82 Interferometric Synthetic Aperture radar (InSAR) provides spatially continuous
83 measurements of surface motions, without instruments on the ground, with precision
84 approaching that obtained from GNSS, and at a resolution that ranges from meters to hundreds of
85 meters [e.g. Bürgmann *et al.*, 2000; Hooper *et al.*, 2012; Hussain *et al.*, 2016; Walters *et al.*,
86 2014; Wright *et al.*, 2001]. However, estimating interseismic strain remains challenging
87 particularly in slowly deforming regions where ground displacements are small and error sources
88 can dominate the differential radar phase [Elliott *et al.*, 2016; Hooper *et al.*, 2012; Shen *et al.*,
89 2019]. Recently, the number of InSAR-capable satellites and volume of associated data have
90 increased and improvements in data quality and processing techniques now permit routine
91 measurements of surface velocities over spatial scales appropriate for studying tectonic plate
92 motions, regional fault systems, and the growth of mountains [e.g. Fattahi and Amelung, 2016;

93 *Grandin et al.*, 2012; *Pagli et al.*, 2014; *Tong et al.*, 2013; *Wang and Wright*, 2012; *Wang et al.*,
94 2019]. In particular, the European Commission's Sentinel-1 constellation, operated by the
95 European Space Agency, with two near-polar orbiting SAR instruments and a revisit period of 6-
96 12 days for most active tectonic belts, has the potential to be a powerful hazard mapping and
97 monitoring tool, which the geoscience community has begun to exploit [e.g. *Elliott et al.*, 2015;
98 *González et al.*, 2015; *Grandin et al.*, 2016; *Shirzaei et al.*, 2017; *Xu et al.*, 2020]. By analyzing
99 large volumes of short-revisit Sentinel-1 data, we can produce displacement time series with
100 reduced impact from atmospheric noise.

101
102 In order to manage and process the large data volumes produced by Sentinel-1, we have
103 developed open-source, automated workflows to efficiently produce interferograms and line-of-
104 sight (LOS) time series and velocities [*Morishita et al.*, 2020], which are valuable for a range of
105 applications. Here we demonstrate our ability to measure large-scale interseismic deformation
106 across Anatolia, an area encompassing $\sim 800,000$ km² and including the highly seismogenic
107 North Anatolian Fault (NAF) Zone. We combine InSAR observations from the first ~ 5 years of
108 the Sentinel-1 mission with published GNSS data to create high-resolution surface velocity and
109 strain rate fields for the region.

110

111 **2. Sentinel-1 Data and LiCSAR processing**

112 We process Sentinel-1 SAR data acquired on 14 overlapping tracks (7 ascending and 7
113 descending) over Anatolia, which were selected to cover the entire region from the intersection
114 of the North and East Anatolian Faults in the east to the Aegean Sea in the west (Figs. 1 and S1).
115 Sentinel-1 data were acquired on every 12-day revisit from the beginning of the Sentinel-1A

116 operational mission in October 2014 and every 6 days since Sentinel-1B became fully
117 operational in September 2016.

118

119 Our InSAR dataset includes 40 spatially and temporally consistent frames (~250 x 250 km)
120 that we define as part of the Sentinel-1 processing system LiCSAR (Figs. 1 and S1) [*González et*
121 *al.*, 2016; *Morishita et al.*, 2020]. By default, we construct temporal baseline interferograms to
122 the six closest acquisitions in time (3 forwards and 3 backwards) and ad hoc additional longer-
123 timespan interferograms to help deal with low coherence due to vegetation in summer months
124 and snow cover in winter months. For each frame, this results in a network of ~600-800
125 interferograms derived from ~200 acquisitions (Fig. S2). Interferograms are downsampled (i.e.
126 multilooked) by a factor of 20 in range and 4 in azimuth producing ground pixels of ~80 x 80 m
127 (resampled to ~100 m spacing during geocoding), and the interferometric phase is unwrapped
128 using a statistical-cost, network-flow algorithm [i.e. SNAPHU; *Chen and Zebker*, 2000; 2001].
129 We partially mitigate atmospheric contributions to apparent displacement signals by applying the
130 iterative troposphere decomposition model implemented in the Generic Atmospheric Correction
131 Online Service for InSAR (GACOS) [*Yu et al.*, 2017; *Yu et al.*, 2018a; *Yu et al.*, 2018b]. On
132 average GACOS reduces the interferogram phase standard deviations by 20-30% (Fig. S3)
133 [*Morishita et al.*, 2020], which should reduce the uncertainty in our LOS velocities by a similar
134 amount compared to the uncorrected velocities. Additional LiCSAR data processing details can
135 be found in the Supporting Information (SI).

136

137 **3. Interseismic Line-of-sight Velocity Field Estimation and Uncertainties**

138 We use LiCSBAS, an open-source InSAR time series analysis package integrated with the
139 LiCSAR processing system [Morishita *et al.*, 2020], to derive InSAR LOS displacement time
140 series and velocities. Our LiCSBAS workflow for Anatolia consists of further downsampling the
141 data by a factor of 10 to a pixel size of ~ 1 km, which is sufficient for large-scale tectonic
142 applications. We perform statistical quality checks [Morishita *et al.*, 2020] prior to the small
143 baseline (SB) inversion, which yields incremental and cumulative displacements and the mean
144 displacement velocity. Despite the short spatial and temporal baselines that generally
145 characterize Sentinel-1 data, gaps in the SB network may still be present due to severe
146 decorrelation (e.g. due to snowfall), extended periods of time with no acquisitions, and after
147 unwrapping consistency checks (Fig. S2). LiCSBAS circumvents this problem by imposing the
148 constraint that displacements are linear in time (i.e. constant velocity) across the gaps [e.g. *Doin*
149 *et al.*, 2011; *López-Quiroz et al.*, 2009]. Finally, we estimate the uncertainty in the velocity from
150 its standard deviation (STD) using the percentile bootstrap method [Efron and Tibshirani, 1986]
151 (Fig. S4) and we mask pixels based on several noise indices (Fig. S5). We also test for potential
152 velocity biases associated with short temporal baseline interferograms in a Sentinel-1 network
153 [e.g. *Ansari et al.*, 2020] by removing 6- and 12-day pairs for one LiCSAR frame prior to
154 LiCSBAS velocity inversion (Fig. S11); the standard deviation of the difference between these
155 results is small (~ 2 mm/yr).

156

157 After LiCSAR/LiCSBAS processing each frame has its own independent reference point for
158 velocity determination (e.g. Fig. S6). We transform the LOS rate maps into a Eurasia-fixed
159 reference frame using a regional GNSS velocity compilation (Fig. 1A and SI) following the
160 method outlined in *Hussain et al.* [2018]; for each frame, we estimate and remove the best-fitting

161 second order polynomial between an interpolated, smoothed GNSS-derived horizontal velocity
162 field projected into the satellite LOS and the InSAR velocities (Fig. 1; SI). This transformation
163 yields a velocity field where the longest wavelength signals are tied to the GNSS data, but it does
164 not affect features at the ~ 100 km length scale and below.

165

166 Fault-perpendicular profiles from the overlap zones of adjacent tracks provide an indication
167 of how well the rate maps agree after the reference frame transformation (Fig. 2). We present one
168 profile taken from ascending-track data crossing the NAF near Ismetpasa and extending
169 southward through the Konya Basin (Figs. 1 and 2) and another taken farther east from
170 descending-track data crossing the NAF and EAF. Both profiles show good agreement between
171 adjacent frames and clear changes in LOS velocity across major fault zones, consistent with the
172 localization of interseismic strain [*Cavalié and Jónsson, 2014; Walters et al., 2014*].

173

174 The bootstrap-derived uncertainties are generally considered to be underestimates
175 particularly if the network is not fully connected [*Morishita et al., 2020*]. Therefore, we also
176 assess LOS velocity uncertainties by calculating the difference between our LOS velocities and a
177 velocity field created by interpolating horizontal GNSS data (see SI), and an associated semi-
178 variogram γ at separation distances h ranging from 0 to 150 km for two off-fault frames (Fig.
179 S6). Our $\sqrt{\gamma(h)}$ values serve as an estimate of velocity uncertainty that is robust up to length
180 scales of ~ 150 km (see SI) [*Bagnardi and Hooper, 2018*]. We use this approach to examine the
181 evolution of uncertainty in our residual LOS measurements by estimating $\sqrt{\gamma(h)}$ for
182 progressively longer time intervals and we find general consistency with the theoretical model
183 derived for error analysis of GNSS time-series data [*Zhang et al., 1997*] for the first ~ 3 years of

184 our Sentinel-1 time series (Fig. S6). At longer time intervals the uncertainty estimates on our
185 Eurasia-fixed velocities reach a minimum of 2-3 mm/yr, likely because our interpolated GNSS
186 velocities are only accurate to this level, whereas the bootstrap-derived estimates continue to
187 decrease with increasing time series length. However, this exercise is useful for determining our
188 ability to measure small amounts of displacement, the time necessary to achieve a certain level of
189 accuracy across different length scales [*Morishita et al.*, 2020], and how detection limits on
190 interseismic velocities evolve with time (Fig. S6).

191

192 As an additional estimate of uncertainty, we also calculate the velocity residuals in the
193 overlap areas for all frames. We do this by assuming horizontal motion only and by correcting
194 for variable LOS by dividing the LOS velocities by the sine of the local incidence angles before
195 multiplying by the sine of the incidence angle at the center of each track [e.g. *Hussain et al.*,
196 2018; *Walters et al.*, 2014]. Histograms of the overlap residuals are approximately Gaussian with
197 means close to zero and standard deviations of 3.1-3.7 mm/yr (Fig. S7). Because LOS velocities
198 are not purely horizontal and due to uncertainties in the GNSS velocities used to transform the
199 LOS information into a Eurasia-fixed reference frame, these values can be considered upper-
200 bound estimates of $\sqrt{2} \times$ the velocity uncertainties for the frames giving an average LOS
201 velocity STD of ~ 2.4 mm/yr.

202

203 **4. East-west and Vertical Surface Velocities for Anatolia**

204 The Eurasia-fixed ascending and descending LOS velocities (Fig. 1) provide a detailed
205 picture of Anatolian surface motions. The most prominent feature is the pronounced gradient in
206 velocity across the NAF, from negligible motion north of the NAF to rapid westward motion of

207 Anatolia relative to Eurasia south of the fault (e.g. Fig. S6). Additional features include localized
 208 regions where there is apparent motion away from the satellite in both ascending and descending
 209 geometries indicating subsidence (Fig. 1B, 1C, and S6).

210

211 To remove some of the ambiguity associated with LOS measurements, we follow the
 212 approach of *Wright et al.* [2004a] and decompose the LOS velocities into east-west and vertical
 213 components for pixels with both ascending and descending information

$$V_{LOS} = [\sin \theta \cos \alpha \quad -\sin \theta \sin \alpha \quad -\cos \theta] \begin{bmatrix} V_E \\ V_N \\ V_U \end{bmatrix}$$

214

215 where V_{LOS} is the Eurasia-fixed LOS velocity, θ is the local radar incidence angle, α is the
 216 azimuth of the satellite heading vector, and $[V_E \ V_N \ V_U]^T$ is a vector with the east, north, and
 217 vertical components of motion, respectively. This equation has three unknowns and we have two
 218 observational constraints in the form of ascending and descending LOS velocities. To calculate
 219 the full 3-D velocity field, we note that both viewing geometries are relatively insensitive to
 220 north-south motion and use the interpolated, smoothed north-south component of the GNSS
 221 velocity field (Fig. 3A) to constrain V_N before solving for V_E and V_U . This approach does not
 222 result in smoothed east-west or vertical velocities because of the LOS north-south insensitivity.

223

224 The resulting decomposed east-west velocity field (Fig. 3) is easier to interpret than the LOS
 225 rate map mosaic and shows large-scale westward motion of Anatolia at a rate of 20-25 mm/yr
 226 relative to Eurasia, with visible strain (a localized velocity gradient) across the entire NAF and
 227 portions of the EAF (Fig. 3B). Along-strike variations in the width of the velocity transition are

228 also evident and correspond to portions of the NAF near Izmit and Ismetpasa where shallow
229 aseismic slip (i.e. creep) has been previously documented (Figs. 1, 3, and S9) [Ambraseys, 1970;
230 Bilham *et al.*, 2016; Cakir *et al.*, 2014; Hussain *et al.*, 2016; Jolivet and Frank, 2020; Kaneko *et*
231 *al.*, 2013; Rousset *et al.*, 2016].

232

233 The decomposed velocity field reveals that portions of Anatolia are experiencing rapid
234 vertical motions. The clearest example is the large zone of subsidence with rates >50 mm/yr
235 surrounding the Konya Basin in south-central Turkey (Figs. 2A, 3C, 3E, S6, and S11), which is
236 attributed to rapid aquifer compaction due to groundwater extraction [Caló *et al.*, 2017; Üstün *et*
237 *al.*, 2015].

238

239 **5. Velocity and Strain Rate Fields from Sentinel-1 InSAR and GNSS Data**

240 To estimate rates of tectonic strain accumulation, we can calculate velocity gradients directly
241 from the decomposed velocity field (see SI; Fig. S10) but our preferred method (see SI for a
242 detailed justification) involves combining InSAR LOS velocity maps with GNSS data and
243 inverting for a velocity and strain rate model using the VELMAP approach [Wang and Wright,
244 2012] (see SI). The technique consists of dividing the study area into a mesh of arbitrary
245 spherical triangles (Fig. S13), assuming the velocity varies linearly (i.e. the strain rate is
246 constant) within each triangle, and using shape functions [England and Molnar, 2005] to solve
247 for the unknown velocities at the vertices of each triangle using the observed InSAR and GNSS
248 measurements. The associated strain and rotation rates are calculated using the spherical
249 approximation equations of Savage *et al.* [2001]. The inversion is regularized using Laplacian
250 smoothing, the strength of which has an impact on the resulting strain rate magnitudes (Figs. S13

251 and S15) including slightly underestimating the strain rates associated with active faults. The
252 approach also does not allow for steps in the velocity field. Additional VELMAP modeling
253 information can be found in the SI.

254

255 Comparison of our preferred Sentinel-1- and GNSS-based model with one based on GNSS
256 data alone (see SI; Figs. 4 and S15) reveals that the inclusion of InSAR data improves the
257 accuracy of the velocity field (Fig. S14) and better captures velocity gradients (and therefore also
258 estimates of strain accumulation) along the major faults (Fig. 2). In the GNSS-only model, the
259 second invariant of the horizontal components of the strain rate tensor (a measure of the total
260 magnitude of the strain rate) indicates the NAF is characterized by a patchy distribution of
261 regions straining at rates >100 nanostrain/yr with even higher strain rates (≥ 150 nanostrain/yr)
262 primarily near clusters of GNSS sites around the western and eastern strands of the fault.
263 Furthermore, central Anatolia is inferred to be essentially undeforming, but in Western Anatolia
264 where earthquake focal mechanisms and the GPS-derived velocity and strain rate fields of *Aktug*
265 *et al.* [2009] show that normal faulting and extension is prevalent, portions of the major grabens
266 are straining at rates >50 nanostrain/yr (Figs. 3 and 4). In contrast, the combined InSAR and
267 GNSS strain rate model shows spatially coherent strain rate magnitudes ≥ 150 nanostrain/yr
268 localized along nearly the entire length of the NAF. The previously identified creeping sections
269 of the fault (Fig. 2B) are also associated with elevated strain rates compared to the GNSS-only
270 map, which exhibits high strain rates in the Izmit region (Fig. 2D) but much lower rates near
271 Isetpasa (Fig. S9). For comparison, we also derive VELMAP strain rates using the alternative
272 Global Strain Rate Model (GSRM) GNSS dataset [see SI; *Kreemer et al.*, 2014], which are

273 characterized by localized patches of high strain along the NAF and in central Anatolia, largely
274 controlled by GNSS site density (Fig. S17).

275

276 Another characteristic of our combined Sentinel-1 InSAR and GNSS result is that the
277 inferred strain rates along the NAF (Fig. 4) are typically half of those stemming from an analysis
278 of Envisat InSAR data by *Hussain et al.* [2018], who took a different approach to estimating
279 strain rate by modeling fault-parallel velocities using 1-D elastic dislocation theory. A main
280 conclusion of *Hussain et al.* [2018] is that strain rates are essentially uniform along the entire
281 length of the fault, implying that the interseismic strain rate is constant in time except in the first
282 decade or two after a major earthquake. We attribute most of the strain rate magnitude
283 discrepancy to the factor of two difference between shear strain rates obtained by computing the
284 full strain rate tensor [*Savage and Burford, 1973; Savage et al., 2001*] and those obtained by
285 taking the spatial derivative of the smoothed, decomposed east-west surface velocity field (i.e.
286 the velocity gradient; Fig. S10; see SI for a detailed explanation) or as in *Hussain et al.* [2018],
287 the gradient of fault-parallel velocity profiles associated with slip on a dislocation in an elastic
288 half space. Once the factor of two is taken in to account, our strain rate magnitudes are still
289 slightly lower than those of *Hussain et al.* [2018] but exhibit a similar first-order pattern
290 suggesting the nearly constant along-strike strain rate is a real and robust feature of the NAF
291 (Fig. S19). This result has important implications as it suggests geodetic strain rate can be used
292 as a long-term estimate of future seismic hazard independent of time since the last earthquake.
293 Second-order differences in strain rate magnitudes are due to the smoothing implemented in
294 VELMAP (Figs. S13, S15, and S19) and not explicitly accounting for fault creep. For example,
295 if we examine the NAF-parallel velocities in a profile that crosses the creeping zone near

296 Ismetpasa, we see that our preferred solution does not capture the sharp velocity gradient evident
297 in the GSRM GNSS velocities (Fig. 2B). Rougher VELMAP models (e.g. Figs. S15 and S16)
298 better reproduce this gradient and return strain rate magnitudes more consistent with the
299 dislocation-based estimates of *Hussain et al.* [2018], but also introduce unacceptably high levels
300 of apparent noise in the central Anatolian strain field (e.g. Fig. S15). Future efforts will focus on
301 developing an improved approach to model regularization that includes spatially variable
302 smoothing and accounts for fault creep.

303

304 While a velocity gradient across portions of the EAF is visible in the decomposed east-west
305 velocities (Fig. 3), our combined strain rate model infers relatively low levels of strain along this
306 fault zone compared to the NAF (Fig. 4), consistent with previous InSAR-based studies [e.g.
307 *Cavalié and Jónsson, 2014; Walters et al., 2014*]. Furthermore, we find appreciable, localized
308 strain accumulation only along the northeastern half of the EAF that is not apparent in the
309 GNSS-only model. This is also where the east-west velocity contrast is most apparent (Fig. 3B).
310 While there is some seismicity associated with the EAF (Fig. 3A), the recently compiled 1900-
311 2012 earthquake catalogue for Turkey [*Kadirioğlu et al., 2018*] indicates that the associated
312 magnitudes and thus total moment release are much lower than along the NAF, supporting the
313 notion that less strain is accumulating along the EAF than the NAF [*Bletery et al., 2020*]. The 24
314 January 2020 M_w 6.7 Elazığ earthquake [*Melgar et al., 2020*] occurred on the short portion of the
315 EAF where we resolve both an east-west velocity gradient and elevated strain rates on the order
316 of ~ 70 nanostrain/yr (Figs. 3 and 4). We infer maximum shear strain and dilatation rates ≥ 100
317 nanostrain/yr associated with active grabens and normal faulting within a broad zone of positive

318 dilatation across the Western Anatolian Extensional Province but relatively low levels of strain
319 along the Central Anatolian Fault Zone (Figs. 3 and 4).

320

321 **6. Conclusions**

322 We have produced, to our knowledge, the largest regional interseismic measurement from
323 InSAR to date, covering a $\sim 800,000$ km² area and the majority of Anatolia. Our strain rate model
324 displays high strains along the major tectonic features, which is consistent with the distribution
325 of seismicity (Figs. 2A and S20). While the availability of abundant GNSS and Sentinel-1
326 InSAR data for Anatolia combined with favorable fault orientations make it ideal for such a
327 study, our results demonstrate the potential of Sentinel-1 data for enhancing the picture of
328 surface deformation and hazard in other regions. A key factor is the equal geographical coverage
329 of Sentinel-1 ascending and descending data, which permits the retrieval of 2D and 3D
330 deformation fields for tectonic zones globally even without the benefit of a dense GNSS dataset
331 (see SI; Fig. S19). In addition, the relatively low uncertainties on Sentinel-1-derived interseismic
332 velocities (Fig. S7) are beneficial for estimating strain across slowly deforming regions and for
333 resolving small temporal changes in deformation throughout the earthquake cycle. Although
334 some challenges still remain for fault systems where the majority of motion is in the north-south
335 direction, Sentinel-1 represents a major improvement over past SAR datasets. This improvement
336 is crucial for monitoring vertical motions from anthropogenic activities and for constraining
337 earthquake hazard, particularly across regions with millennial earthquake recurrence intervals,
338 where seismic hazard assessments based on incomplete historical earthquake records can
339 dangerously underestimate the true hazard [*Stein et al.*, 2012; *Stevens and Avouac*, 2016].

340

341 **Acknowledgements**

342 We thank Marco Bagnardi and Thomas Ingleby for helping JRW get up to speed with InSAR
343 upon his arrival in Leeds, Philip England and Gregory Houseman for insights regarding deriving
344 velocities and strain rates from geodetic data, and Emma Hatton and Nicholas Greenall for their
345 contributions to LiCSAR development. We also thank Romain Jolivet, Lucy Flesch, and an
346 anonymous reviewer for comments that helped us improve the manuscript. We are grateful to
347 Tom Merry for help with code debugging. This research was supported by the Natural
348 Environmental Research Council (NERC) through the Centre for the Observation and Modelling
349 of Earthquakes, Volcanoes and Tectonics, the Looking inside the Continents from Space large
350 grants to Oxford (NE/K011006/1), Leeds (NE/K010867/1), and Newcastle (NE/K010794/1)
351 Universities, and the Earthquakes without Frontiers project (EwF_NE/J02001X/1_1). JRW is
352 also supported by the German Research Foundation (DFG) and the State of Brandenburg, TJW
353 by the Royal Society, YM by the Japan Society for the Promotion of Science Overseas Research
354 Fellowship, and HW by the NSFC (41672205). GMT [Wessel *et al.*, 2013] was used to create the
355 figures presented in this paper. All interferograms are available for download from
356 comet.nerc.ac.uk/comet-lics-portal, the time series analysis software LiCSBAS can be accessed
357 via *Morishita et al.* [2020], and information regarding accessing GACOS corrections can be
358 found in *Yu et al.* [2018b].

359

360

361

362

363

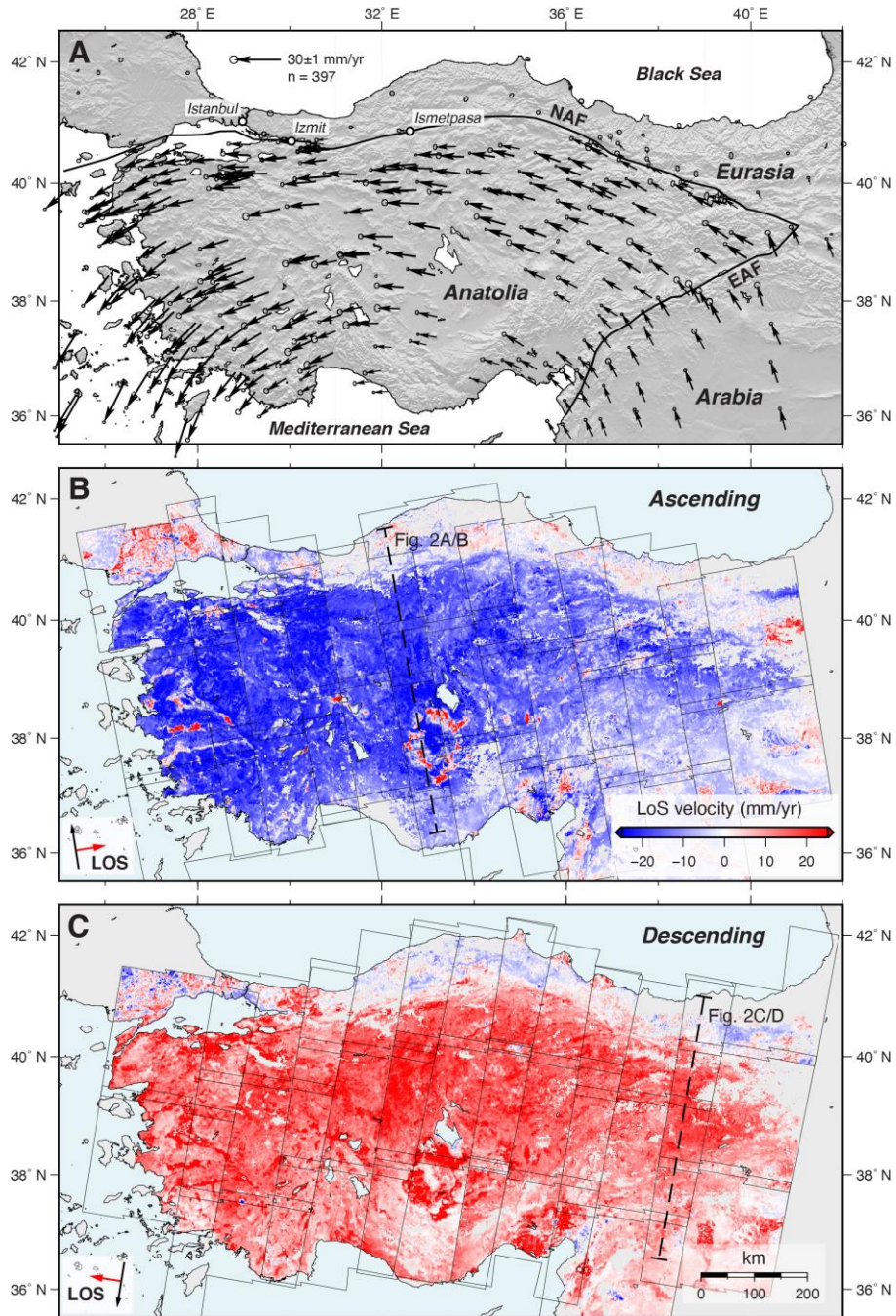
364

365

366

367

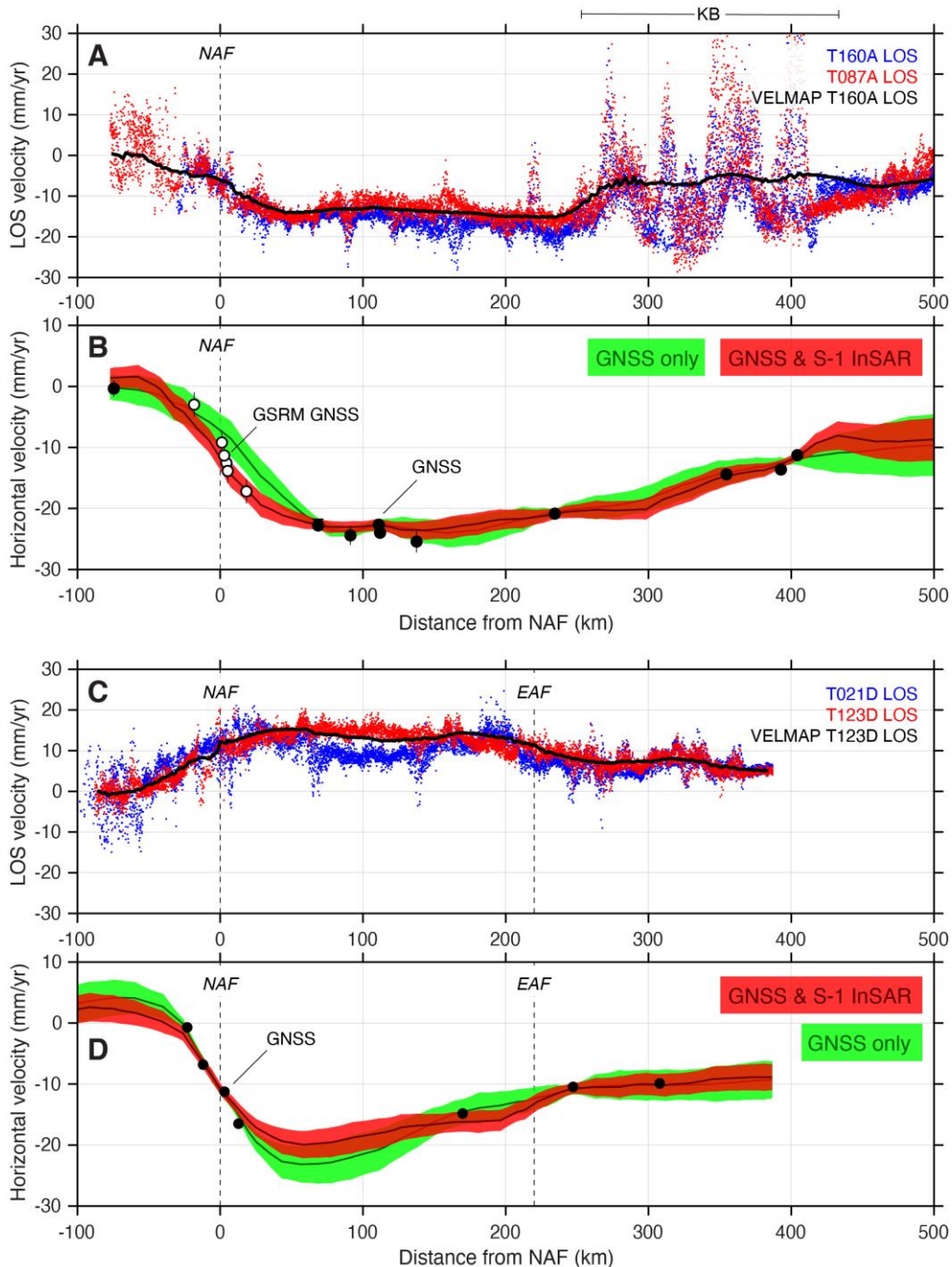
368



369

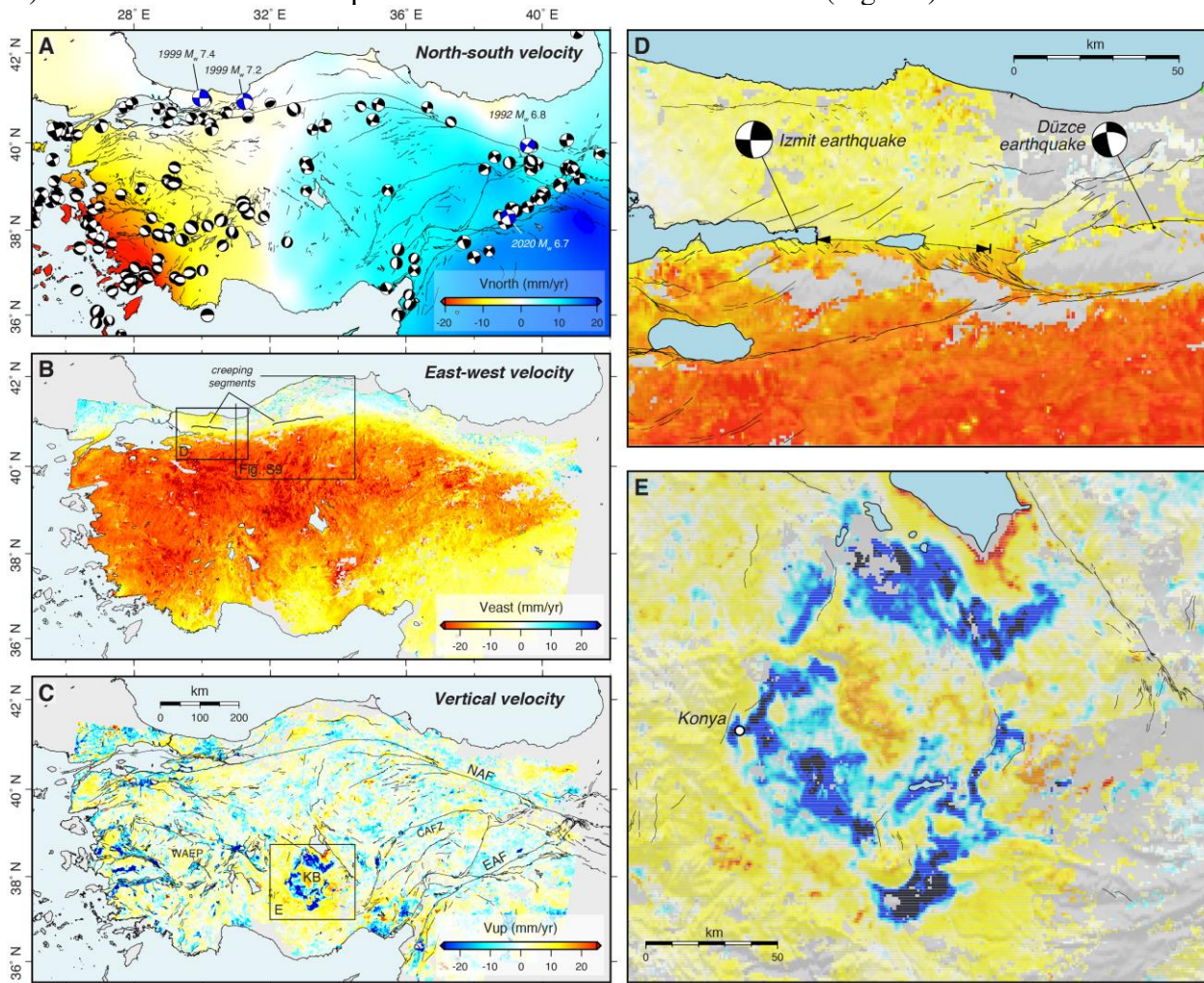
370
 371
 372
 373
 374
 375
 376
 377
 378
 379

Fig. 1. Tectonic setting of Anatolia and interseismic surface velocities in a Eurasia-fixed reference frame. (A) GNSS velocity vectors from *England et al.* [2016] and *Nocquet* [2012], illuminating the counterclockwise rotation of Anatolia and Arabia relative to Eurasia. Black lines indicate the main strands of the North Anatolian Fault (NAF) and East Anatolian Fault (EAF). (B) Ascending and (C) descending track Sentinel-1 line-of-sight (LOS) velocities with LiCSAR frame boundaries. Negative (blue) and positive (red) values indicate relative motion towards and away from the satellite, respectively. Color scale is the same in (B) and (C). Fig. 2 profile locations are indicated in (B) and (C).



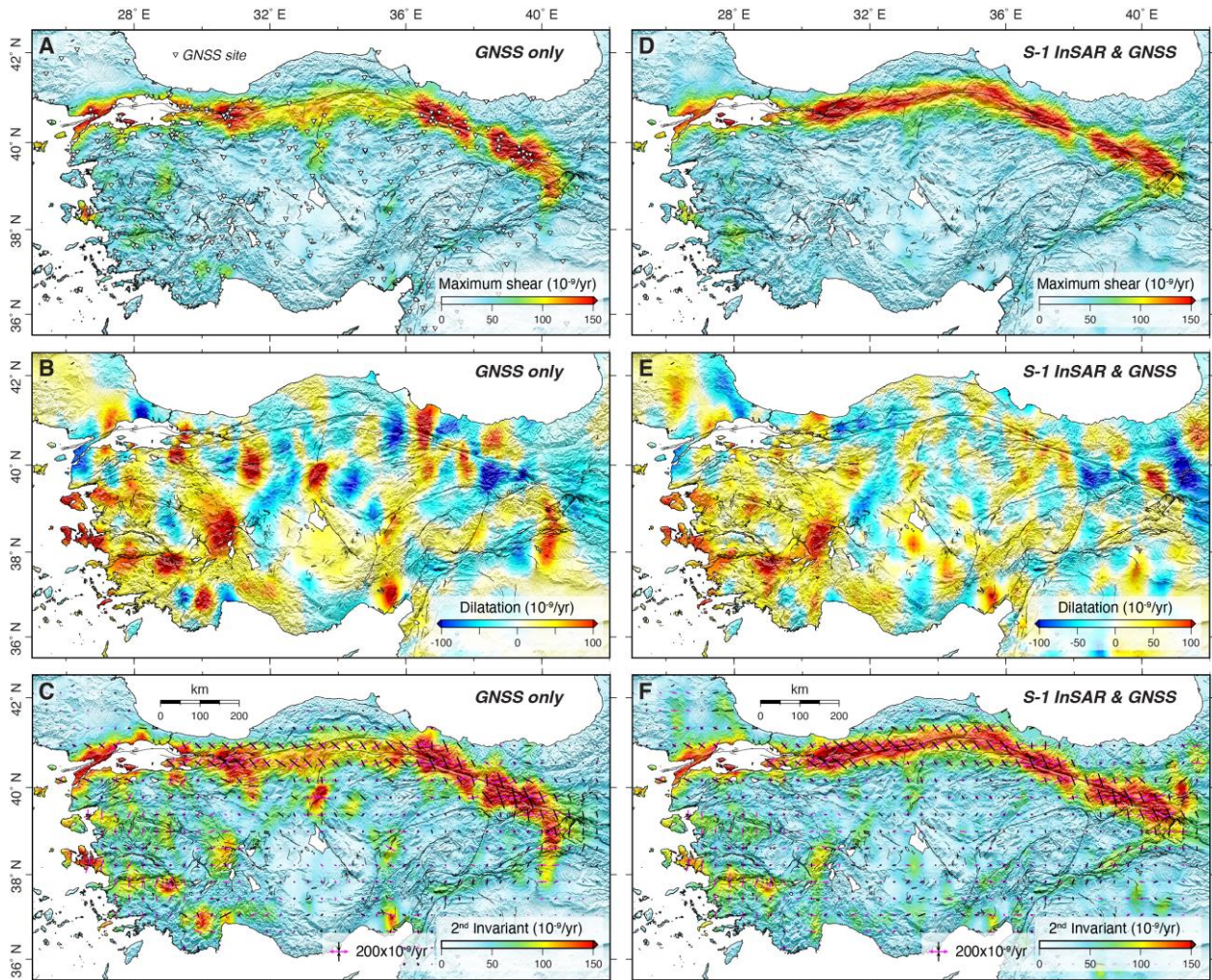
380

381
 382 **Fig. 2.** Velocity profiles for Anatolia. (A) InSAR LOS velocities within 25 km of the NAF-
 383 crossing profile shown in Fig. 1B for overlapping tracks T160A (blue) and T087A (red). The
 384 black line is the mean VELMAP LOS velocity for T087A. (B) Red band shows combined
 385 Sentinel-1 InSAR and GNSS profile-perpendicular horizontal velocities with 1σ errors from our
 386 preferred VELMAP model. Green band represents the GNSS-only model. Filled circles and 2σ
 387 error bars are the GNSS velocities (white from GSRM are not used in the VELMAP inversion).
 388 The southern portion of the profile crosses the Konya Basin (KB; see main text and Fig. S8). (C-
 389 D) Same as above but for a profile that crosses the NAF and EAF (Fig. 1C).



390
 391
 392 **Fig. 3.** Horizontal and vertical surface velocities for the Anatolian region. (A) Interpolated north-
 393 south velocities based on the GNSS data and shallow earthquake focal mechanisms from the
 394 GCMT catalogue [Ekström *et al.*, 2012]. Recent large labeled events include the 1999 M_w 7.4
 395 Izmit, the 1999 M_w 7.2 Düzce, the 1992 M_w 6.8 Erzincan, and the 2020 M_w 6.7 Elazığ
 396 earthquakes. (B) East-west and (C) vertical velocities decomposed from the combined Sentinel-1
 397 LOS and GNSS north-south velocities. Previously identified creeping portions of the NAF are
 398 indicated in (B). Also shown are close-up views of the decomposed surface velocities for (D)
 399 a section of the NAF surrounding the Izmit and Düzce earthquakes with the creeping section
 400 determined by Aslan *et al.* [2019] indicated with arrows and (E) the Konya Basin region with

401 areas subsiding at rates ≥ 50 mm/yr shown in black. Semi-transparent SRTM topography hill-
 402 shades are draped over the velocity fields shown in the close-ups. See Fig. S9 for a detailed view
 403 of the creeping section near Ismetpasa. Thin black lines in (A), (C), (D), and (E) are active faults
 404 from [Emre *et al.*, 2018]. KB=Konya Basin. CAFZ=Central Anatolian Fault Zone.
 405 WAEP=Western Anatolian Extensional Province.
 406
 407
 408
 409
 410



411
 412

413 **Fig. 4** VELMAP strain rate fields for Anatolia. (A) Maximum shear strain rate, (B) dilatation
 414 rate, and (C) second invariant of the strain rate tensor, derived using GNSS data only. White
 415 triangles in (A) are GNSS site locations. (D-F) Strain rate components from a joint inversion of
 416 the GNSS and Sentinel-1 LOS velocities. Black and magenta bars in (C) and (F) represent the
 417 contractional and extensional principal strain rates, respectively. The maximum shear strain rates
 418 imply focused deformation along the NAF and EAF and wholesale positive dilatation across
 419 western Anatolia is indicative of extension whereas short-wavelength features in the dilatation
 420 field likely reflect anthropogenic vertical signals that result in subsurface expansion and
 421 contraction and contribute to noisy patches in the 2nd invariant estimates. See Figs. S15 and S19

422 for additional components of the strain rate tensor and a comparison with seismicity rates,
423 respectively.

424
425
426
427
428
429
430
431
432

433 **References**

434 Aktug, B., et al. (2009), Deformation of western Turkey from a combination of permanent and
435 campaign GPS data: Limits to block-like behavior, *Journal of Geophysical Research: Solid*
436 *Earth*, 114(B10).

437 Ambraseys, N. N. (1970), Some characteristic features of the Anatolian fault zone,
438 *Tectonophysics*, 9(2), 143-165.

439 Ansari, H., F. De Zan, and A. Parizzi (2020), *Study of Systematic Bias in Measuring Surface*
440 *Deformation with SAR Interferometry*.

441 Argus, D. F., R. G. Gordon, and C. DeMets (2011), Geologically current motion of 56 plates
442 relative to the no-net-rotation reference frame, *Geochemistry, Geophysics, Geosystems*, 12(11).

443 Aslan, G., C. Lasserre, Z. Cakir, S. Ergintav, S. Özarparci, U. Dogan, R. Bilham, and F. Renard
444 (2019), Shallow Creep Along the 1999 Izmit Earthquake Rupture (Turkey) From GPS and High
445 Temporal Resolution Interferometric Synthetic Aperture Radar Data (2011–2017), *Journal of*
446 *Geophysical Research: Solid Earth*, 124(2), 2218-2236.

447 Bagnardi, M., and A. Hooper (2018), Inversion of Surface Deformation Data for Rapid Estimates
448 of Source Parameters and Uncertainties: A Bayesian Approach, *Geochemistry, Geophysics,*
449 *Geosystems*, 19(7), 2194-2211.

450 Bilham, R., et al. (2016), Surface creep on the North Anatolian Fault at Ismetpasa, Turkey,
451 1944–2016, *Journal of Geophysical Research: Solid Earth*, 121(10), 7409-7431.

452 Bird, P., D. D. Jackson, Y. Y. Kagan, C. Kreemer, and R. S. Stein (2015), GEAR1: A Global
453 Earthquake Activity Rate Model Constructed from Geodetic Strain Rates and Smoothed
454 Seismicity, *Bulletin of the Seismological Society of America*.

455 Bletery, Q., O. Cavalie, J.-M. Nocquet, and T. Ragon (2020), Distribution of interseismic
456 coupling along the North and East Anatolian Faults inferred from InSAR and GPS data, *Earth*
457 *and Space Science Open Archive*.

458 Bürgmann, R., P. A. Rosen, and E. J. Fielding (2000), Synthetic Aperture Radar Interferometry
459 to Measure Earth's Surface Topography and Its Deformation, *Annual Review of Earth and*
460 *Planetary Sciences*, 28(1), 169-209.

- 461 Cakir, Z., S. Ergintav, A. M. Akoğlu, R. Çakmak, O. Tatar, and M. Meghraoui (2014), InSAR
462 velocity field across the North Anatolian Fault (eastern Turkey): Implications for the loading and
463 release of interseismic strain accumulation, *Journal of Geophysical Research: Solid Earth*,
464 *119*(10), 7934-7943.
- 465 Caló, F., D. Notti, J. P. Galve, S. Abdikan, T. Görüm, A. Pepe, and F. Balik Şanlı (2017),
466 DInSAR-Based Detection of Land Subsidence and Correlation with Groundwater Depletion in
467 Konya Plain, Turkey, *Remote Sensing*, *9*(1), 83.
- 468 Cavalié, O., and S. Jónsson (2014), Block-like plate movements in eastern Anatolia observed by
469 InSAR, *Geophysical Research Letters*, *41*(1), 26-31.
- 470 Cetin, E., Z. Cakir, M. Meghraoui, S. Ergintav, and A. M. Akoglu (2014), Extent and
471 distribution of aseismic slip on the Ismetpaşa segment of the North Anatolian Fault (Turkey)
472 from Persistent Scatterer InSAR, *Geochemistry, Geophysics, Geosystems*, *15*(7), 2883-2894.
- 473 Chaussard, E., R. Bürgmann, H. Fattahi, R. M. Nadeau, T. Taira, C. W. Johnson, and I. Johanson
474 (2015), Potential for larger earthquakes in the East San Francisco Bay Area due to the direct
475 connection between the Hayward and Calaveras Faults, *Geophysical Research Letters*, *42*(8),
476 2734-2741.
- 477 Chen, C. W., and H. A. Zebker (2000), Network approaches to two-dimensional phase
478 unwrapping: intractability and two new algorithms, *J. Opt. Soc. Am. A*, *17*(3), 401-414.
- 479 Chen, C. W., and H. A. Zebker (2001), Two-dimensional phase unwrapping with use of
480 statistical models for cost functions in nonlinear optimization, *J. Opt. Soc. Am. A*, *18*(2), 338-
481 351.
- 482 Doin, M.-P., F. Lodge, S. Guillaso, R. Jolivet, C. Lasserre, G. Ducret, R. Grandin, E. Pathier, and
483 V. Pinel (2011), Presentation of the small baseline NSBAS processing chain on a case example:
484 The Etna deformation monitoring from 2003 to 2010 using Envisat data, in *FRINGE*, edited,
485 Frascati, Italy.
- 486 Efron, B., and R. Tibshirani (1986), Bootstrap Methods for Standard Errors, Confidence
487 Intervals, and Other Measures of Statistical Accuracy, *Statist. Sci.*, *1*(1), 54-75.
- 488 Ekström, G., M. Nettles, and A. M. Dziewoński (2012), The global CMT project 2004–2010:
489 Centroid-moment tensors for 13,017 earthquakes, *Physics of the Earth and Planetary Interiors*,
490 *200-201*, 1-9.
- 491 Elliott, J. R., R. J. Walters, and T. J. Wright (2016), The role of space-based observation in
492 understanding and responding to active tectonics and earthquakes, *Nature Communications*, *7*,
493 13844.
- 494 Elliott, J. R., A. J. Elliott, A. Hooper, Y. Larsen, P. Marinkovic, and T. J. Wright (2015),
495 Earthquake monitoring gets boost from new satellite, *Eos, Transactions American Geophysical*
496 *Union*, *96*.

- 497 Emre, Ö., T. Y. Duman, S. Özalp, F. Şaroğlu, Ş. Olgun, H. Elmacı, and T. Çan (2018), Active
 498 fault database of Turkey, *Bulletin of Earthquake Engineering*, 16(8), 3229-3275.
- 499 England, P., and P. Molnar (2005), Late Quaternary to decadal velocity fields in Asia, *Journal of*
 500 *Geophysical Research: Solid Earth*, 110(B12), n/a-n/a.
- 501 England, P. C., G. A. Houseman, and J. M. Nocquet (2016), Constraints from GPS
 502 measurements on the dynamics of deformation in Anatolia and the Aegean, *Journal of*
 503 *Geophysical Research: Solid Earth*.
- 504 Fattahi, H., and F. Amelung (2016), InSAR observations of strain accumulation and fault creep
 505 along the Chaman Fault system, Pakistan and Afghanistan, *Geophysical Research Letters*,
 506 43(16), 8399-8406.
- 507 Goldstein, R. M., and C. L. Werner (1998), Radar interferogram filtering for geophysical
 508 applications, *Geophysical Research Letters*, 25(21), 4035-4038.
- 509 González, P. J., E. Hatton, R. J. Walters, A. J. Hooper, and T. J. Wright (2016), Sentinel-1
 510 InSAR time series processing: one year and counting, paper presented at The Living Planet
 511 Symposium, Czech Republic.
- 512 González, P. J., M. Bagnardi, A. J. Hooper, Y. Larsen, P. Marinkovic, S. V. Samsonov, and T. J.
 513 Wright (2015), The 2014–2015 eruption of Fogo volcano: Geodetic modeling of Sentinel-1
 514 TOPS interferometry, *Geophysical Research Letters*, 42(21), 9239-9246.
- 515 Grandin, R., E. Klein, M. Métois, and C. Vigny (2016), Three-dimensional displacement field of
 516 the 2015 Mw8.3 Illapel earthquake (Chile) from across- and along-track Sentinel-1 TOPS
 517 interferometry, *Geophysical Research Letters*, 43(6), 2552-2561.
- 518 Grandin, R., M.-P. Doin, L. Bollinger, B. Pinel-Puysegue, G. Ducret, R. Jolivet, and S. N.
 519 Sapkota (2012), Long-term growth of the Himalaya inferred from interseismic InSAR
 520 measurement, *Geology*, 40(12), 1059-1062.
- 521 Hearn, E. H. (2003), What can GPS data tell us about the dynamics of post-seismic
 522 deformation?, *Geophysical Journal International*, 155(3), 753-777.
- 523 Hooper, A., D. Bekaert, K. Spaans, and M. Arıkan (2012), Recent advances in SAR
 524 interferometry time series analysis for measuring crustal deformation, *Tectonophysics*, 514-517,
 525 1-13.
- 526 Hussain, E., A. Hooper, T. J. Wright, R. J. Walters, and D. P. S. Bekaert (2016), Interseismic
 527 strain accumulation across the central North Anatolian Fault from iteratively unwrapped InSAR
 528 measurements, *Journal of Geophysical Research: Solid Earth*, 121(12), 9000-9019.
- 529 Hussain, E., T. J. Wright, R. J. Walters, D. P. S. Bekaert, R. Lloyd, and A. Hooper (2018),
 530 Constant strain accumulation rate between major earthquakes on the North Anatolian Fault,
 531 *Nature Communications*, 9(1), 1392.

- 532 Jolivet, R., and W. B. Frank (2020), The Transient and Intermittent Nature of Slow Slip, *AGU*
533 *Advances*, 1(1), e2019AV000126.
- 534 Jolivet, R., C. Lasserre, M. P. Doin, G. Peltzer, J. P. Avouac, J. Sun, and R. Dailu (2013), Spatio-
535 temporal evolution of aseismic slip along the Haiyuan fault, China: Implications for fault
536 frictional properties, *Earth and Planetary Science Letters*, 377-378, 23-33.
- 537 Kadirioğlu, F., R. Kartal, T. Kılıç, D. Kalafat, T. Duman, T. Eroğlu Azak, S. Özalp, and Ö. Emre
538 (2018), An improved earthquake catalogue ($M \geq 4.0$) for Turkey and its near vicinity (1900–
539 2012), *Bulletin of Earthquake Engineering*, 16, 3317-3338.
- 540 Kaneko, Y., Y. Fialko, D. T. Sandwell, X. Tong, and M. Furuya (2013), Interseismic
541 deformation and creep along the central section of the North Anatolian Fault (Turkey): InSAR
542 observations and implications for rate-and-state friction properties, *Journal of Geophysical*
543 *Research: Solid Earth*, 118(1), 316-331.
- 544 Kreemer, C., G. Blewitt, and E. C. Klein (2014), A geodetic plate motion and Global Strain Rate
545 Model, *Geochemistry, Geophysics, Geosystems*, 15(10), 3849-3889.
- 546 Lindsey, E. O., Y. Fialko, Y. Bock, D. T. Sandwell, and R. Bilham (2014), Localized and
547 distributed creep along the southern San Andreas Fault, *Journal of Geophysical Research: Solid*
548 *Earth*, 119(10), 7909-7922.
- 549 López-Quiroz, P., M.-P. Doin, F. Tupin, P. Briole, and J.-M. Nicolas (2009), Time series
550 analysis of Mexico City subsidence constrained by radar interferometry, *Journal of Applied*
551 *Geophysics*, 69(1), 1-15.
- 552 Loveless, J. P., and B. J. Meade (2011), Partitioning of localized and diffuse deformation in the
553 Tibetan Plateau from joint inversions of geologic and geodetic observations, *Earth and*
554 *Planetary Science Letters*, 303(1), 11-24.
- 555 Melgar, D., A. Ganas, T. Taymaz, S. Valkaniotis, B. W. Crowell, V. Kapetanidis, V. Tsironi, S.
556 Yolsal-Cevikbilen, and T. Ocalan (2020), Rupture Kinematics of January 24, 2020 Mw 6.7
557 Doğanyol-Sivrice, Turkey Earthquake on the East Anatolian Fault Zone Imaged by Space
558 Geodesy, *EarthArXiv*.
- 559 Molnar, P. (1979), Earthquake recurrence intervals and plate tectonics, *Bulletin of the*
560 *Seismological Society of America*, 69(1), 115-133.
- 561 Morishita, Y., M. Lazecky, T. J. Wright, J. R. Weiss, J. R. Elliott, and A. Hooper (2020),
562 LiCSBAS: An Open-Source InSAR Time Series Analysis Package Integrated with the LiCSAR
563 Automated Sentinel-1 InSAR Processor, *Remote Sensing*, 12(3), 424.
- 564 Nocquet, J.-M. (2012), Present-day kinematics of the Mediterranean: A comprehensive overview
565 of GPS results, *Tectonophysics*, 579, 220-242.

- 566 Pagli, C., H. Wang, T. J. Wright, E. Calais, and E. Lewi (2014), Current plate boundary
567 deformation of the Afar rift from a 3-D velocity field inversion of InSAR and GPS, *Journal of*
568 *Geophysical Research: Solid Earth*, 119(11), 8562-8575.
- 569 Parsons, B., T. Wright, P. Rowe, J. Andrews, J. Jackson, R. Walker, M. Khatib, M. Talebian, E.
570 Bergman, and E. R. Engdahl (2006), The 1994 Sefidabeh (eastern Iran) earthquakes revisited:
571 new evidence from satellite radar interferometry and carbonate dating about the growth of an
572 active fold above a blind thrust fault, *Geophysical Journal International*, 164(1), 202-217.
- 573 Prats-Iraola, P., R. Scheiber, L. Marotti, S. Wollstadt, and A. Reigber (2012), TOPS
574 Interferometry With TerraSAR-X, *IEEE Transactions on Geoscience and Remote Sensing*,
575 50(8), 3179-3188.
- 576 Reilinger, R., and S. McClusky (2011), Nubia–Arabia–Eurasia plate motions and the dynamics
577 of Mediterranean and Middle East tectonics, *Geophysical Journal International*, 186(3), 971-
578 979.
- 579 Rollins, C., and J.-P. Avouac (2019), A Geodesy- and Seismicity-Based Local Earthquake
580 Likelihood Model for Central Los Angeles, *Geophysical Research Letters*, 46(6), 3153-3162.
- 581 Rousset, B., R. Jolivet, M. Simons, C. Lasserre, B. Riel, P. Milillo, Z. Çakir, and F. Renard
582 (2016), An aseismic slip transient on the North Anatolian Fault, *Geophysical Research Letters*,
583 43(7), 3254-3262.
- 584 Savage, J. C., and R. O. Burford (1973), Geodetic determination of relative plate motion in
585 central California, *Journal of Geophysical Research (1896-1977)*, 78(5), 832-845.
- 586 Savage, J. C., W. Gan, and J. L. Svarc (2001), Strain accumulation and rotation in the Eastern
587 California Shear Zone, *Journal of Geophysical Research: Solid Earth*, 106(B10), 21995-22007.
- 588 Schmidt, D. A., and R. Bürgmann (2003), Time-dependent land uplift and subsidence in the
589 Santa Clara valley, California, from a large interferometric synthetic aperture radar data set,
590 *Journal of Geophysical Research: Solid Earth*, 108(B9).
- 591 Shen, L., A. Hooper, and J. Elliott (2019), A Spatially Varying Scaling Method for InSAR
592 Tropospheric Corrections Using a High-Resolution Weather Model, *Journal of Geophysical*
593 *Research: Solid Earth*, 124(4), 4051-4068.
- 594 Shirzaei, M., R. Bürgmann, and E. J. Fielding (2017), Applicability of Sentinel-1 Terrain
595 Observation by Progressive Scans multitemporal interferometry for monitoring slow ground
596 motions in the San Francisco Bay Area, *Geophysical Research Letters*, 44(6), 2733-2742.
- 597 Smith, B. R., and D. T. Sandwell (2006), A model of the earthquake cycle along the San Andreas
598 Fault System for the past 1000 years, *Journal of Geophysical Research: Solid Earth*, 111(B1),
599 n/a-n/a.
- 600 Stein, S., R. J. Geller, and M. Liu (2012), Why earthquake hazard maps often fail and what to do
601 about it, *Tectonophysics*, 562-563, 1-25.

- 602 Stevens, V. L., and J.-P. Avouac (2016), Millenary Mw > 9.0 earthquakes required by geodetic
603 strain in the Himalaya, *Geophysical Research Letters*, 43(3), 1118-1123.
- 604 Tong, X., D. T. Sandwell, and B. Smith-Konter (2013), High-resolution interseismic velocity
605 data along the San Andreas Fault from GPS and InSAR, *Journal of Geophysical Research: Solid*
606 *Earth*, 118(1), 369-389.
- 607 Torres, R., et al. (2012), GMES Sentinel-1 mission, *Remote Sensing of Environment*, 120, 9-24.
- 608 Üstün, A., et al. (2015), Land subsidence in Konya Closed Basin and its spatio-temporal
609 detection by GPS and DInSAR, *Environmental Earth Sciences*, 73(10), 6691-6703.
- 610 Walters, R. J., B. Parsons, and T. J. Wright (2014), Constraining crustal velocity fields with
611 InSAR for Eastern Turkey: Limits to the block-like behavior of Eastern Anatolia, *Journal of*
612 *Geophysical Research: Solid Earth*, 119(6), 5215-5234.
- 613 Walters, R. J., P. C. England, and G. A. Houseman (2017), Constraints from GPS measurements
614 on the dynamics of the zone of convergence between Arabia and Eurasia, *Journal of*
615 *Geophysical Research: Solid Earth*, 122(2), 1470-1495.
- 616 Wang, H., and T. J. Wright (2012), Satellite geodetic imaging reveals internal deformation of
617 western Tibet, *Geophysical Research Letters*, 39(7).
- 618 Wang, H., T. J. Wright, J. Liu-Zeng, and L. Peng (2019), Strain Rate Distribution in South-
619 Central Tibet From Two Decades of InSAR and GPS, *Geophysical Research Letters*, 46(10),
620 5170-5179.
- 621 Wei, M., D. Sandwell, and B. Smith-Konter (2010), Optimal combination of InSAR and GPS for
622 measuring interseismic crustal deformation, *Advances in Space Research*, 46(2), 236-249.
- 623 Weiss, J. R., et al. (2019), Illuminating subduction zone rheological properties in the wake of a
624 giant earthquake, *Science Advances*.
- 625 Wessel, P., W. H. F. Smith, R. Scharroo, J. Luis, and F. Wobbe (2013), Generic Mapping Tools:
626 Improved Version Released, *Eos, Transactions American Geophysical Union*, 94(45), 409-410.
- 627 Wright, T. (2016), The earthquake deformation cycle, *Astronomy & Geophysics*, 57, 4.20-24.26.
- 628 Wright, T. J., B. Parsons, and E. Fielding (2001), Measurement of interseismic strain
629 accumulation across the North Anatolian Fault by satellite radar interferometry, *Geophysical*
630 *Research Letters*, 28(10), 2117-2120.
- 631 Wright, T. J., B. E. Parsons, and Z. Lu (2004a), Toward mapping surface deformation in three
632 dimensions using InSAR, *Geophysical Research Letters*, 31(1), n/a-n/a.
- 633 Wright, T. J., B. Parsons, P. C. England, and E. J. Fielding (2004b), InSAR Observations of Low
634 Slip Rates on the Major Faults of Western Tibet, *Science*, 305(5681), 236-239.

- 635 Wright, T. J., J. R. Elliott, H. Wang, and I. Ryder (2013), Earthquake cycle deformation and the
636 Moho: Implications for the rheology of continental lithosphere, *Tectonophysics*, 609, 504-523.
- 637 Xu, X., D. T. Sandwell, and B. Smith-Konter (2020), Coseismic Displacements and Surface
638 Fractures from Sentinel-1 InSAR: 2019 Ridgecrest Earthquakes, *Seismological Research Letters*.
- 639 Yu, C., N. T. Penna, and Z. Li (2017), Generation of real-time mode high-resolution water vapor
640 fields from GPS observations, *Journal of Geophysical Research: Atmospheres*, 122(3), 2008-
641 2025.
- 642 Yu, C., Z. Li, and N. T. Penna (2018a), Interferometric synthetic aperture radar atmospheric
643 correction using a GPS-based iterative tropospheric decomposition model, *Remote Sensing of*
644 *Environment*, 204, 109-121.
- 645 Yu, C., Z. Li, N. T. Penna, and P. Crippa (2018b), Generic Atmospheric Correction Model for
646 Interferometric Synthetic Aperture Radar Observations, *Journal of Geophysical Research: Solid*
647 *Earth*, 123(10), 9202-9222.
- 648 Zhang, J., Y. Bock, H. Johnson, P. Fang, S. Williams, J. Genrich, S. Wdowinski, and J. Behr
649 (1997), Southern California Permanent GPS Geodetic Array: Error analysis of daily position
650 estimates and site velocities, *J Geophys Res-Sol Ea*, 102(B8), 18035-18055.
651